

DETECTION OF OH ABSORPTION AGAINST PSR B1849+00

SNEŽANA STANIMIROVIĆ

Radio Astronomy Lab, UC Berkeley, 601 Campbell Hall, Berkeley, CA 94720
sstanimi@astro.berkeley.edu

JOEL M. WEISBERG

Department of Physics and Astronomy, Carleton College, Northfield, MN 55057

JOHN M. DICKEY

Department of Astronomy, University of Minnesota, 116 Church St. SE, Minneapolis, MN 55455

ANTON DE LA FUENTE, KATHRYN DEVINE, ABIGAIL HEDDEN

Department of Physics and Astronomy, Carleton College, Northfield, MN 55057

STUART B. ANDERSON

Department of Astronomy, MS 18-34, California Institute of Technology, Pasadena, CA 91125

Draft version October 30, 2018

ABSTRACT

We have searched for OH absorption against seven pulsars using the Arecibo telescope. In both OH mainlines (at 1665 and 1667 MHz), deep and narrow absorption features were detected toward PSR B1849+00. In addition, we have detected several absorption and emission features against B33.6+0.1, a nearby supernova remnant (SNR). The most interesting result of this study is that a pencil-sharp absorption sample against the PSR differs greatly from the large-angle absorption sample observed against the SNR. If both the PSR and the SNR probe the same molecular cloud then this finding has important implications for absorption studies of the molecular medium, as it shows that the statistics of absorbing OH depends on the size of the background source. We also show that the OH absorption against the PSR most likely originates from a small (< 30 arcsec) and dense ($> 10^5$ cm⁻³) molecular clump.

Subject headings: line: profiles — pulsars: individual (B1849+00) — supernovae: individual (B33.6+0.1) — ISM: molecules — ISM: structure

1. INTRODUCTION

Much information concerning the interstellar medium (ISM) has been gleaned from studies of the absorption of pulsar signals by neutral hydrogen at $\lambda \sim 21$ cm. Kinematic distances derived from absorption spectra, in combination with pulsar dispersion measures, have determined the electron density throughout the plane of the Galaxy (Weisberg et al. 1995). Combination of absorption and emission spectra along the same line-of-sight allows us to determine optical depth and inferred spin temperature of the cold neutral gas in front of the pulsar (Weisberg et al. 1979; Koribalski et al. 1995). Particularly interesting application of pulsar absorption studies is by Frail et al. (1994) who found temporal variations in pulsar absorption spectra, suggesting structure in the absorbing HI clouds at the tens-of-AU scale (the tiny-scale atomic structure or TSAS). The origin and properties of TSAS are still a great puzzle. Observations suggest that these features have pressure > 300 times greater than the standard pressure of the cold neutral medium, being far from in a pressure equilibrium with the surrounding medium, unless they possess an extremely extended geometry (Heiles 1997).

Another interesting issue was addressed by Dickey et al. (1981) who studied the existence of very small scale structure in the HI optical depth distribution. They compared abundance of HI absorption lines in various optical depth intervals measured against both continuum extragalactic sources, with typical angular sizes of $1''$ to $3'$, and against pulsars. As both sets of sources showed similar abundance

of HI absorption lines they concluded that the angular size of background sources does not influence the optical depth measurements in HI, at least over the angular size range $0.001''$ to $3'$.

As pointed out by Dickey et al. (1981), pulsars are particularly powerful background sources for emission-absorption studies because the solid angle subtended by their continuum emission is extremely small. Although scattering in the ISM broadens their apparent size, the effective diameter of the line-of-sight volume is still on AU scales. This means that absorption spectra against pulsars probe needle-thin samples of the ISM. Another great advantage which pulsars offer as background sources for such studies, is that they turn on and off, thus allowing the absorption and emission spectra to be measured without moving the telescope. This eliminates the errors introduced in the absorption spectrum by small scale spatial variations in the emission.

Motivated by pulsars' unique capabilities for studying the ISM, and in an effort to extend their use to molecular medium, we measured the absorption spectra of several pulsars at the wavelength of the hydroxyl radical (OH), $\lambda \sim 18$ cm. The only previous attempts to determine pulsar OH absorption spectra were by Galt (1974), who did not detect absorption in the spectrum of PSR B0329+54, and by Slysh (1972), who observed B0329+54, B0450-18, B0525+21, B0740-28, B1642-03, and B1749-28; and detected OH absorption at 1667 MHz toward the latter one. As pulsar emission is weak at 18 cm OH absorption measurements are quite difficult and require a very sensitive in-

strument. We used the Arecibo telescope and detected OH absorption against one of our sources – PSR B1849+00. The line-of-sight toward B1849+00 is particularly interesting as it passes right through the Galactic plane and is very close to a nearby supernova remnant (SNR) G33.6+0.1. In this paper we focus on a detailed comparison between OH absorption spectra toward B1849+00 and G33.6+0.1.

This paper is organized as follows. We start in Section 2 with a brief background on the two objects of interest in the paper, B1849+00 and G33.6+0.1. Section 3 describes our Arecibo OH observations and data processing. To learn more about the large-scale distribution of molecular gas and compare it with OH we used the Steward Observatory’s 12-m telescope to map a $25' \times 25'$ region around G33.6+0.1 in $^{12}\text{CO}(1-0)$; these observations are also summarized in Section 3. Detected OH absorption spectra toward B1849+00 and G33.6+0.1 are presented and analyzed in Section 4 and Section 5. The $^{12}\text{CO}(1-0)$ distribution is presented in Section 6. In Section 7 we discuss the main result of this paper – the great difference between OH absorption spectra measured against the continuum emission from B1849+00 and G33.6+0.1 separately along the same line-of-sight. We present two geometrical scenarios to explain this difference and investigate several possible implications. We conclude in Section 8.

2. BACKGROUND ON PSR B1849+00 AND SNR G33.6+0.1

PSR B1849+00 is a low-latitude, $(l, b) = (33.5, 0.0)$, long-period (2.18 s) pulsar discovered by Clifton & Lyne (1986). What is particularly interesting about this object is its very high dispersion measure of $(680 \pm 60) \text{ cm}^{-3} \text{ pc}$ (Clifton et al. 1988). HI absorption measurements towards B1849+00 were obtained by Clifton et al. (1988) who established that the PSR is located beyond the tangent point (8.4 kpc) but not significantly beyond the Solar circle (19 kpc). The electron density model by Lyne et al. (1985) predicted a distance of 14.5 kpc to B1849+00. The new electron density model by Cordes & Lazio (2002) places the PSR at a dispersion measure distance of (8.4 ± 1.7) kpc, while the most recent model for the Galactic rotation by Fich et al. (1989) places a HI kinematic lower limit to its distance of 7 kpc.

PSR B1849+00 is located eight arcmin south of the center of the SNR G33.6+0.1 (also known as Kes 79, 4C00.70, HC13). Two extragalactic point sources, 1849+005 and 1850+009 are located 14 arcmin south-west and 14 arcmin north, respectively, of G33.6+0.1. G33.6+0.1 is a shell type SNR with diameter of about 10 arcmin (Caswell et al. 1981). 21-cm continuum observations by Frail & Clifton (1989) confirmed its morphology and a slightly larger diameter of ~ 16 arcmin. HI absorption measurements towards B1849+00, G33.6+0.1, 1849+005 and 1850+009 by Frail & Clifton (1989) concluded that 1849+005 and 1850+009 are indeed extragalactic sources, and that the SNR lies in front of the PSR, at the distance of (10 ± 2) kpc. This distance was determined by scaling the PSR distance of 14.5 kpc by the ratio of HI optical depth integrals of the SNR and the PSR. We note though that this method is very uncertain especially at low Galactic

latitudes where any change in optical depth profiles along nearby lines-of-sight is more likely to be due to density or temperature variations in the absorbing cloud than due to one of the background objects being more distant.

Several studies have investigated a possible relationship between B1849+00 and G33.6+0.1. Han (1997) suggested that the two objects are related and that B1849+00 was born inside G33.6+0.1. However, very recently, Seward et al. (2002) detected a compact object with Chandra, right in the center of G33.6+0.1, which seems to be a much stronger candidate for the neutron star created in the SNR explosion.

The unusually high dispersion measure of B1849+00 and its proximity to G33.6+0.1 motivated several authors to investigate whether the SNR is (partially) responsible for the interstellar scattering along the PSR’s line-of-sight. In particular, Spangler et al. (1986) investigated whether the turbulence toward the PSR could be driven by diffuse shock acceleration upstream of the SNR boundary. The uncertain distances to the two objects hindered conclusive results. Frail & Clifton (1989) were also unable to distinguish whether the scattering occurs from a thin screen provided by the SNR or from a more general type of Galactic turbulence.

There were several previous investigations of molecular gas in the direction of G33.6+0.1 (Turner 1979; Scoville et al. 1987; Green 1989; Green & Dewdney 1992). OH absorption and emission features were observed by Turner (1979) and Green (1989). $^{12}\text{CO}(1-0)$ observations by Scoville et al. (1979) found a molecular cloud in the same direction. Green & Dewdney (1992) observed bright and extended HCO^+ emission in the eastern portion of the SNR at velocities corresponding to the molecular cloud and concluded that the SNR is most likely interacting with the cloud. Green et al. (1997) detected emission at 1720 MHz associated with the SNR using the Parkes telescope, however compact maser emission was not detected with the VLA observations by Koralesky et al. (1998).

3. OBSERVATIONS AND DATA PROCESSING

3.1. Arecibo OH Observations

OH observations were undertaken in early January 2000 toward seven pulsars, using the Arecibo 305-m telescope¹. The observed pulsars were: B1737+13, B1849+00, B1933+16, B2016+28, B1944+17, B1915+13 and B1929+10. These pulsars were selected from the Princeton Pulsar Catalogue (Taylor et al. 1993) as having low galactic latitude, a reasonably high flux density at 21-cm and previously detected sharp HI absorption features. The OH absorption was detected only against one of our observed sources – PSR B1849+00. A marginal detection was found in direction of B1915+13 which requires further confirmation.

3.1.1. Observing Technique

The Gregorian feed was used with the “L-band wide” receiver (with frequency range 1.12 – 1.73 GHz). The illuminated part of the 305-m dish covers an area of about 210×240 m, resulting in a beam FWHM of approximately

¹ The Arecibo Observatory is part of the National Astronomy and Ionosphere Center, operated by Cornell University under a cooperative agreement with the National Science Foundation.

$2'.6 \times 3'.0$ at 1.6 GHz. The Caltech Baseband Recorder (CBR; Jenet et al. (1997)) was used as a fast-sampling backend, with a total bandwidth of 10 MHz at each of two orthogonal circular polarizations, simultaneously covering both OH mainlines at 1665.4018 and 1667.3590 MHz. The raw complex voltage data samples were recorded every 100 ns and stored directly on DLT tapes for further analysis. Observations were undertaken in blocks of ‘ON’-frequency scans, centered on 1664.4 MHz and having duration of about 30 min, and ‘OFF’-frequency scans, centered at 1666.4 MHz, required to perform frequency switching to flatten baselines, lasting about 5 min. The observing frequency was corrected for the changing Doppler shift of the observatory with respect to the local standard of rest (LSR) at each frequency change. In particular, PSR B1849+00 is observable at Arecibo only for about one hour each day, and at the zenith angle of about 18 degrees. The system temperature at this zenith angle was about 40 K. In total, 2.8 hours were spent for this object on the ‘ON’-frequency scans, and about 40 min on the ‘OFF’-frequency scans. All data tapes were sent to Caltech’s Center for Advance Computation and Research (CACR) for further processing.

3.1.2. Off-line data processing

The fast-sampled raw data were Fourier-transformed to provide a sequence of dedispersed spectra, each consisting of 2048 frequency channels across a 10 MHz total bandwidth for the two orthogonal polarizations. (See Jenet et al. (1997) for details of the algorithm.) The spectra have frequency resolution of 4.9 kHz, or velocity resolution of 0.9 km s^{-1} , without any smoothing. These spectra were then accumulated modulo the apparent pulsar period into one of 128 pulse-rotational-phase bins. The five- to thirty-minute scan is now represented by a data cube of temperature as a function of frequency and pulse phase.

The next stage of data processing involved extraction of ‘ON’-pulse and ‘OFF’-pulse spectra from the 3-dimensional data cube for each scan. Our software finds the pulsar pulse in the cube, and weights (by T_{PSR}^2) and accumulates those spectra gathered during the pulse into a raw “pulsar-on” spectrum and those measured between pulses into a “pulsar-off” spectrum. Two types of spectra of astrophysical interest are then formed. The grand pulsar absorption spectrum (see Fig. 1), which depicts the pulsar signal alone (as absorbed by any intervening OH), takes advantage of the pulsed nature of pulsar radiation. The grand pulsar absorption spectrum is created by generating the “pulsar-on” – “pulsar-off” spectrum for a scan; then doing frequency switching to flatten the baseline; and finally accumulating all such spectra with a weight again proportional to T_{PSR}^2 . The grand “pulsar-off” spectrum (see Fig. 2), which registers all emission and absorption lying in the telescope beam during the time that the pulsar signal is not present, is created by summing all scans’ “pulsar-off” spectra, and then fitting and removing a polynomial to flatten the baseline. (We decided to fit a polynomial to the grand “pulsar-off” spectrum, rather than doing frequency switching, because of the great complexity of the spectrum; multiple emission and absorption features were present at both OH mainlines, with the line separation of 1.95 MHz and the frequency switching offset of 2 MHz.)

The normalized grand pulsar absorption spectra, at 1665 and 1667 MHz, are in units of $I(v)/I_0 = e^{-\tau(v)}$, the optical depth of the intervening OH, and do not require any further calibration. The grand “pulsar-off” spectra are in units of brightness temperature and need to be calibrated. As sources of known temperature were not observed for the flux calibration purpose, we calibrated these spectra by comparing them with previous OH observations towards G33.6+0.1, obtained by Turner (1979) using the NRAO 140-ft telescope (FWHM of 18.8 arcmin). A constant, overall, conversion factors were estimated for both 1665 and 1667 MHz lines to scale our spectra to match those presented by Turner (1979). The spectra were then scaled down by a factor of 1.6 as the PSR is located south of the SNR where continuum emission is weaker, therefore the brightness temperature covered by the Arecibo beam is lower than the brightness temperature at the center of the SNR. This additional scaling factor was estimated from HI contours presented in Fig. 1 of Frail & Clifton (1989). The rms noise in the resultant spectra agrees within 25% with the expected theoretical noise level calculated for the given integration time, bandwidth and the system temperature (including the SNR contribution). The optical depth was calculated using:

$$\tau(v) = -\ln\left(\frac{T_{\text{B}}(v)}{T_{\text{B}}^{\text{cont}}} + 1\right) \quad (1)$$

where brightness temperature of continuum emission $T_{\text{B}}^{\text{cont}} \sim 4 \text{ K}$ was assumed.

3.2. 12-m CO Observations

G33.6+0.1 was previously mapped in $^{12}\text{CO}(1-0)$ with the 12-m telescope by Green (1989), however these data are not easily accessible in electronic form. We re-observed a $25' \times 15'$ region around G33.6+0.1. Observations were obtained in December 2002. Absolute on-the-fly mapping was performed with a scanning rate of $60''/\text{sec}$ and a reference position being RA $19^{\text{h}} 00^{\text{m}}$, Dec $-01^{\circ} 30'$ (B1950). The planet Mars was used for pointing and focus. Two filter banks and the digital millimeter autocorrelator were used simultaneously to record data for two orthogonal polarizations, resulting in final velocity resolutions of 1.3, 2.6 and 0.1 km s^{-1} per channel. The data reduction was performed in the AIPS package. Line-free channels were used for continuum subtraction. Data were gridded using the SDGRD task. The rms noise level is 0.4 K per 1.3 km s^{-1} wide channels. At 115 GHz the telescope FWHM is 55 arcsec. Main beam efficiency is 0.62 and forward spillover and efficiency is 0.72. To convert from recorded T_{R} to brightness temperature T_{B} multiplication by 1.16 is required. To further convert to flux density multiplication by the antenna gain, 33 Jy K^{-1} , is required (Helfer & et al. 2003).

4. PULSAR OH ABSORPTION SPECTRUM TOWARD PSR B1849+00

Fig. 1 (first and second panel) shows the pulsar OH absorption spectra, at 1665 and 1667 MHz, toward B1849+00. At both frequencies, narrow absorption lines were detected at velocity of about 102 km s^{-1} . This is the first successful OH absorption, to our knowledge, in

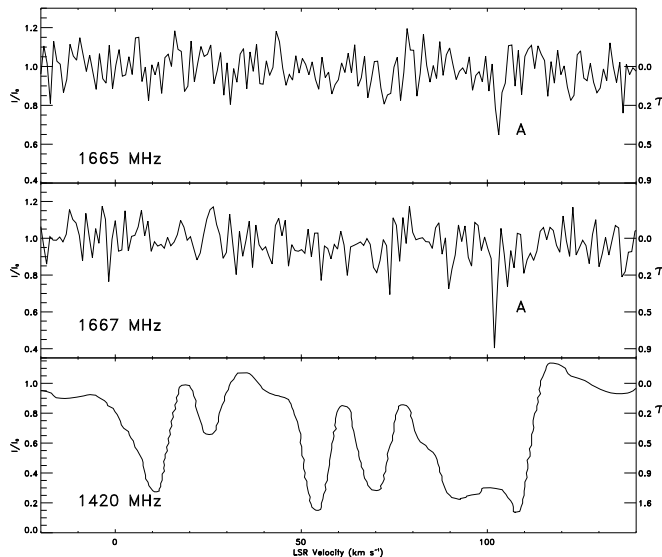


FIG. 1.— Pulsar absorption spectra toward B1849+00 at 1665 and 1667 MHz (first and second panel). The 1420 MHz absorption spectrum against the PSR from Clifton et al. (1988) (third panel). Each spectrum is a difference spectrum between “pulsar-on” and “pulsar-off” spectra, and hence shows absorption produced against the PSR only.

both OH mainlines detected toward any pulsar. The optical depth noise level is 0.08. The detected absorption lines have an intensity of $> 5\text{-}\sigma$.

As described above in Section 3.1.2, these spectra depict the pulsar signal *alone* being absorbed by intervening OH. It is important to note that emission and absorption due to any other source, astrophysical or instrumental, has been eliminated via the differencing procedure that generated these spectra. The units on the left-hand axis on Fig. 1 are for the normalized pulsar intensity (I/I_0), while the right-hand axis shows the optical depth of OH lying between the pulsar and Earth ($\tau = -\ln(I/I_0)$). Several additional weak absorption features could be present in the OH spectra presented in Fig. 1. In particular, there may be a hint of an absorption feature seen at 1667 MHz around velocity of 75 km s^{-1} where a strong CO emission is found (see Fig. 2). However, we concentrate in this paper only on more than $3\text{-}\sigma$ detections. The last panel in Fig. 1 shows the HI absorption of signals from PSR B1849+00, adopted from Clifton et al. (1988).

The absorption system shown in Fig. 1, which we label as ‘A’, seems to have an unusually high optical depth. Typical OH absorption found in the surveys against extragalactic sources has $\langle \tau_{1667} \rangle \sim 0.05$ and $\langle \text{FWHM} \rangle \sim 1 \text{ km s}^{-1}$ (Dickey et al. 1981; Colgan et al. 1989; Liszt & Lucas 1996). Higher optical depths are quite rare and are found close to SNRs and/or HII regions (Goss 1968; Manchester & Gordon 1971; Yusef-Zadeh et al. 2003).

We fitted Gaussian functions to the PSR optical depth profiles, $\tau = \tau_{\text{max}} \exp[-4 \ln 2 (v - v_0)^2 / \text{FWHM}^2]$ and Table 1 lists the derived parameters. Columns 3 – 5 give τ_{max} , v_0 and FWHM, which are the peak height, velocity center and full width at half maximum, respectively. Column 6 gives the equivalent width, $\text{EW} = \int \tau dv$, and column 7 gives the ratio of equivalent widths for 1667 and 1665 MHz lines, $R_\tau = \text{EW}(1667)/\text{EW}(1665)$. $R_\tau = 1.8$ for thermal-

ized level populations of any optical depth (Dickey et al. 1981). Column 8 gives the ratio of OH column density N_{OH} to the excitation temperature T_{ex} , determined by:

$$\frac{N_{\text{OH}}}{T_{\text{ex}}} = \frac{C_0}{f} \int \tau dv \quad (2)$$

where $C_0 = 4.0 \times 10^{14}$, for the 1665 MHz line, and $C_0 = 2.24 \times 10^{14} \text{ cm}^{-2} \text{ K}^{-1} (\text{km s}^{-1})^{-1}$ for the 1667 MHz line. The OH solid angle filling factor f is assumed to be unity for these calculations.

Absorption features seen in Fig. 1 (see also Table 1) are very narrow with the velocity FWHM of 1.5 and 1.1 km s^{-1} , respectively. In addition, central velocities of feature ‘A’ at 1665 and 1667 MHz differ by about 1 km s^{-1} . This is very surprising result. There is no instrumental or processing step, to our knowledge, that could cause such an offset. The two OH main line rest frequencies are known to 100 Hz accuracy (Ter Meulen & Dymanus 1972), while the offset between central frequencies of feature ‘A’ at 1665 and 1667 MHz is 5.6 kHz. The 1665 and 1667 MHz spectra are actually two chunks of a single 10 MHz wide spectrum, making an instrumental channel offset problem unlikely. It is also hard to explain this offset as being due to an astronomical reason. The only possible reason we can think of are shock effects that could somehow cause population difference in the lower states of the two OH main transitions. However, we are not aware of theoretical models of this phenomenon. Certainly, further observations with higher velocity resolution are necessary to confirm this offset.

5. PULSAR OFF SPECTRUM

Fig. 2 (first and second panel) shows the “pulsar-off” spectrum (see Section 3.1.2). As the SNR G33.6+0.1 is centered only 8 arcmin from B1849+00 and its diameter is ~ 16 arcmin (from Frail & Clifton 1989, their Fig. 1), while the Arecibo telescope FWHM at 1666 MHz is

TABLE 1
FITTED OH PARAMETERS.

Feature	Transition (MHz)	τ_{\max}	v_0 (km s $^{-1}$)	FWHM $_v$ (km s $^{-1}$)	EW (km s $^{-1}$)	R_τ	$\frac{N_{\text{OH}}}{T_{\text{ex}}}$ 10 14 (cm $^{-2}$ K $^{-1}$)
Pulsar							
A	1665	0.4 ± 0.1	103.0 ± 0.2	1.5 ± 0.4	0.8	1.5	3.2
	1667	0.9 ± 0.1	102.0 ± 0.1	1.1 ± 0.2	1.2		2.7
SNR							
A	1665	0.010 ± 0.002	101.6 ± 0.9	11.9 ± 1.3	0.14		1.7
	1665	0.049 ± 0.002	104.4 ± 0.1	4.7 ± 0.2	0.28		
B	1665	0.003 ± 0.001	8.7 ± 2.2	10.4 ± 3.8	0.04	1.0	0.5
	1665	0.021 ± 0.002	11.9 ± 0.1	3.0 ± 0.3	0.08	2.7	
A	1667	0.016 ± 0.003	94.0 ± 0.4	4.7 ± 0.9	0.09		0.8
	1667	0.021 ± 0.001	101.8 ± 0.5	9.8 ± 1.3	0.25		
B	1667	0.007 ± 0.003	9 ± 3	5 ± 4	0.04		0.6
	1667	0.066 ± 0.009	11.7 ± 0.1	2.8 ± 0.2	0.22		
C	1667	-0.012 ± 0.003	70.1 ± 1.3	6.6 ± 1.6	-0.1		
	1667	-0.030 ± 0.006	72.6 ± 0.1	2.7 ± 0.5	-0.1		

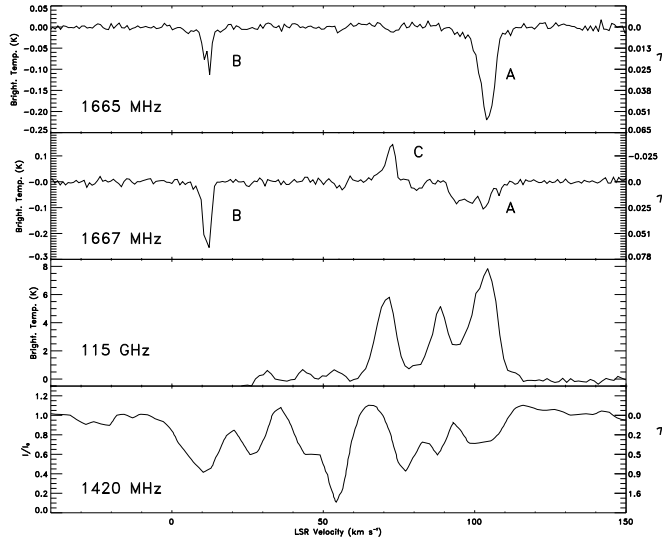


FIG. 2.— The “pulsar-off” spectrum toward B1849+00 at 1665 (first panel) and 1667 (second panel). Absorption and emission features seen in this spectrum, and labeled as ‘A’, ‘B’ and ‘C’, are observed against SNR B33.6+0.1 which is partially covered by the Arecibo beam. The $^{12}\text{CO}(1-0)$ emission spectra, obtained with the 12-m telescope in direction toward the PSR and averaged over the whole Arecibo beam, $\sim 3'$, (third panel). The 1420 MHz spectrum (fourth panel), is the HI absorption spectrum toward the SNR, from Frail & Clifton (1989).

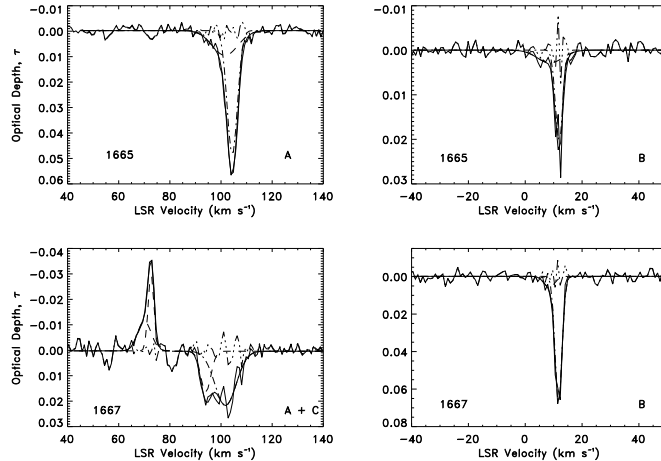


FIG. 3.— Gaussian fits to the OH spectral lines, observed in Fig. 2, against the SNR (thin solid line): wide Gaussian component (dashed line), narrow Gaussian component (dot-dashed line), final fit as a sum of the two components (thick solid line), and residuals (dot-dot-dashed line).

$2.6' \times 3.0'$, the absorption features in this spectrum are effectively produced by intervening OH lying in front of G33.6+0.1. The third panel on Fig. 2 shows $^{12}\text{CO}(1-0)$ emission in the direction of B1849+00 integrated over the Arecibo beam. The fourth panel in Fig. 2 shows the 1420 MHz absorption spectrum toward G33.6+0.1 from Frail & Clifton (1989).

The “pulsar-off” spectra show two absorption systems, centered at about 102 and 10 km s^{-1} , observed in both OH mainlines. The first one, ‘A’, has been already seen in the PSR absorption spectrum. We label the second one as ‘B’. In addition, there is an emission feature, ‘C’, seen at about 70 km s^{-1} . It is immediately obvious that these absorption features differ greatly, in both peak intensity and linewidth, from features seen in the pulsar absorption spectra in Figure 1. In particular, feature ‘A’ in the 1667 MHz line is almost 15 times wider and 30 times shallower than its corresponding feature in the PSR absorption spectrum.

We fitted Gaussian functions to optical depth profiles of features ‘A’, ‘B’ and ‘C’ and results are shown in Table 1. In all cases at least two Gaussian functions were required as observed profiles are broad. Usually, a wider Gaussian component is necessary to fit line wings, where optical depth decreases more gradually. The fitted Gaussian components and their corresponding residuals are shown in Fig. 3. Absolute values for the peak optical depth are at least 10 times lower than for the pulsar absorption spectra, but are similar to values obtained in several OH surveys toward extragalactic sources (Dickey et al. 1981; Colgan et al. 1989; Liszt & Lucas 1996). The FWHM of narrow Gaussian components is typically 3-5 km s^{-1} , while for the wider component is ~ 10 km s^{-1} .

Wide absorption/emission profiles could be caused by blending of molecular clumps along the line of sight (Marscher et al. 1991; Marscher & Stone 1994). Another possible cause of wide absorption profiles is propagation of a C-type shock through a molecular cloud, which could occur in the case of a cloud-SNR interaction. Flower & Pineau des Forets (1998) modeled OH absorption line pro-

files in the presence of C-type shocks and found double peaks arising from contributions from both the host (quiescent) and shocked gas. Their double components have comparable peak values but the quiescent one is significantly narrower than the shocked one. Fig. 3 and Table 1 show that feature ‘A’ at 1667 MHz is reminiscent of the C-type model profiles. This particular OH absorption line was interpreted previously as a signature of an interaction between the SNR and a molecular cloud (Green 1989; Green & Dewdney 1992). However, in three other cases the wider Gaussian component is associated with the line wing only and does not resemble profiles expected from C-type shocks.

In the case of feature ‘A’ wide Gaussian components at both 1665 and 1667 MHz agree well in central velocity and FWHM, we then use their equivalent widths to estimate $R_\tau = 1.5$. Narrow components have very different central velocity. Similarly, for feature ‘B’ narrow Gaussian components agree well in central velocity and FWHM, and have $R_\tau = 2.7$. Wider Gaussian components for feature ‘B’ have the same central velocity but significantly different FWHM, in this case $R_\tau = 1.0$.

6. CO DISTRIBUTION

Fig. 4 shows $^{12}\text{CO}(1-0)$ emission at different LSR velocities. The CO data presented here complement data published by Green & Dewdney (1992) by covering a wider velocity range. A large molecular cloud (with size of > 25 arcmin) is seen between 97 and 113 km s^{-1} that extends over the whole continuum distribution of G33.6+0.1, see $^{12}\text{CO}(1-0)$ integrated intensity image in Fig. 5. This cloud was first cataloged by Scoville et al. (1987) who estimated its average linear size of ~ 40 pc and a mean molecular hydrogen density of ~ 180 cm^{-3} . The CO emission is particularly strong on the west part of the SNR. At several positions along this side Green & Dewdney (1992) also found strong HCO^+ emission which was interpreted as being due to an interaction between the SNR and the molecular cloud. The cloud is elongated along the Galactic plane (in the direction from the north-west to the south-east)

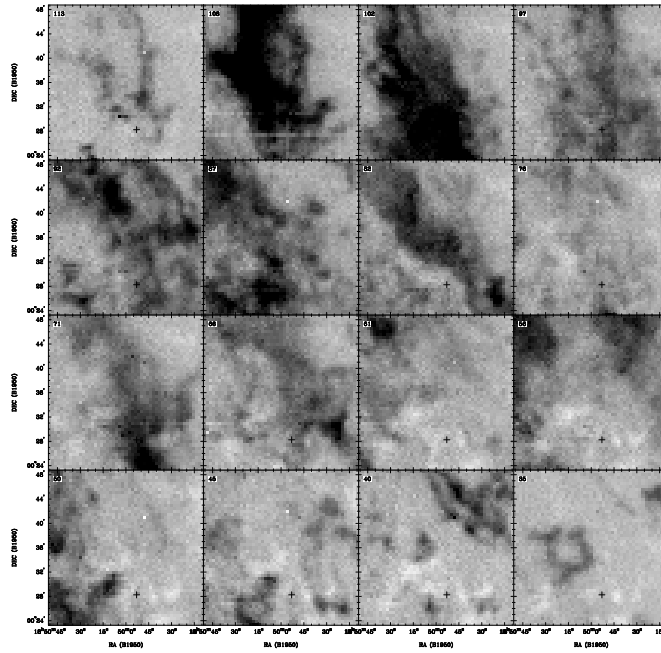


FIG. 4.— Right ascension-declination images of $^{12}\text{CO}(1-0)$ emission at different LSR velocities, given in the top left corner of each panel, obtained with the 12-m telescope. The grey-scale range is -2.3 to 7.5 K, with a linear transfer function. Position of B1849+00 is given with a cross.

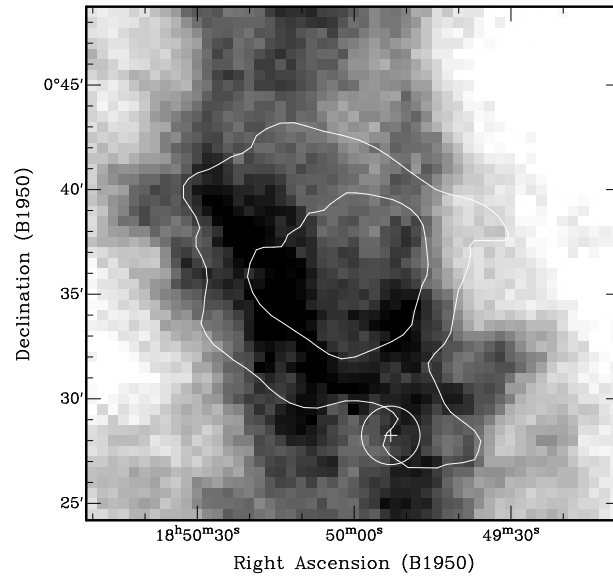


FIG. 5.— Integrated $^{12}\text{CO}(1-0)$ intensity image obtained with the 12-m telescope along with 21-cm continuum contours of the SNR from the VLA. Integrated velocity range covers 95 to 113 km s^{-1} . The overlaid contours are from the the 21-cm continuum image of G33.6+0.1 from Frail & Clifton (1989), at 2 and 16 K levels of brightness temperature. The PSR position as shown with a cross and the Arecibo beam is shown with a circle (FWHM of ~ 3 arcmin).

and has somewhat sharper edge on the lower latitude side.

An interesting loop-like feature is seen around 113 km s⁻¹, extended along the Galactic plane. Around 92 km s⁻¹ a higher latitude cloud is seen that transforms into a long filament running parallel to the plane at about 82 km s⁻¹. Although these are low sensitivity observations a wealth of small scale molecular features is found, particularly around 92 and 40–42 km s⁻¹.

Two small clouds, probably belonging to larger complexes, are seen at 56 km s⁻¹, RA 18^h 49^m 40^s, Dec 00° 40′ 00″, and at ~48–50 km s⁻¹, RA 18^h 50^m 08^s Dec 00° 30′ 0.14″. The peak brightness temperature of clouds is 7.5 and 8 K and they both lie in the direction of the continuum emission associated with G33.6+0.1. Interestingly, Turner (1979) observed an OH absorption feature at 57 km s⁻¹ in 1667 MHz line, accompanied with an emission feature at 60 km s⁻¹ in 1665 MHz lines. Observations by Green (1989) at 1667 MHz showed a flip from an absorption at 55 km s⁻¹ to an emission at 60 km s⁻¹. An interesting donut-like feature is seen around 35 km s⁻¹.

Figure 5 shows the integrated ¹²CO(1-0) intensity distribution over velocity range 95 to 113 km s⁻¹, near our feature ‘A’. Contours of the 21-cm continuum image of G33.6+0.1 by Frail & Clifton (1989) are also overlaid. The mean velocity of the cloud is 106 km s⁻¹, no velocity gradient is found.

7. DISCUSSION

What is particularly striking about the OH absorption data presented in this paper is that the difference in the observed optical depths (line shape, width and peak) in the PSR absorption spectrum (Fig. 1) and the “pulsar-off” spectrum (Fig. 2, 1st and 2nd panel) is so great. The PSR absorption spectrum shows absorption by the intervening OH against the pulsar continuum emission *alone*, while the “pulsar-off” spectrum shows absorption produced against the continuum emission from G33.6+0.1 *alone* within the Arecibo beam. In other words, spectra in Figs. 1 and 2 show two different absorption features along *the same* line-of-sight and with the same central velocity around 103 km s⁻¹. In particular, the absorption features seen in the PSR absorption spectra at 1665 and 1667 MHz are deep and narrow, but with the ratio of equivalent widths for 1665 and 1667 MHz lines being very close to 5:9. The line ratio suggests that the observed absorption spectra are not the result of an instrumental or processing artefact, but that originate from molecular gas along the line of sight toward the PSR.

From Table 1, $N_{\text{OH}}/T_{\text{ex}} \sim 3 \times 10^{14} \text{ cm}^{-2} \text{ K}^{-1}$ for feature ‘A’ in the PSR absorption spectra. It is typically assumed that $T_{\text{ex}} \sim 5 \text{ K}$ for clouds unassociated with HII regions, and around 10 K for clouds associated with HII regions (Bourke et al. 2001). Liszt & Lucas (1996) have found that gas seen in OH absorption has typically $T_{\text{ex}} \sim 4 \text{ K}$, while gas seen in OH emission is warmer with $T_{\text{ex}} \sim 7\text{--}13 \text{ K}$. With assumption of $T_{\text{ex}} \sim 5\text{--}10 \text{ K}$, we estimate $N_{\text{OH}} \sim \text{few} \times 10^{15} \text{ cm}^{-2}$. Under assumption that column densities of OH and hydrogen (HI+H₂) are related with $N_{\text{H}} \sim 10^8 N_{\text{OH}}$, we get $N_{\text{H}} \sim \text{few} \times 10^{23} \text{ cm}^{-2}$ for this feature. This is higher than what is usually sampled by OH (Bourke et al. 2001).

In Section 6 we showed that a large molecular cloud is seen in the SNR and the PSR direction. The line shapes

(see Section 5) and previous work by Green (1989) and Green & Dewdney (1992) suggest that the SNR is most likely interacting with the molecular cloud. To explain the large difference in absorption optical depths against the PSR and SNR we investigate two possible geometrical scenarios.

7.1. An additional molecular cloud is located in front of the PSR yet behind the SNR

It is possible that absorption features seen in the PSR absorption spectrum and the “pulsar-off” spectrum are not related physically. This could happen in the case where the sharp and deep absorption lines, seen in the PSR absorption spectra, come from an additional molecular cloud located in front of the PSR yet behind the SNR (see Fig. 6 case 1 for a graphical representation). The broad OH absorption lines in the “pulsar-off” spectrum are, most likely, a result of the interaction between the SNR and the molecular cloud, while the narrow absorption lines are not associated with the cloud-SNR interaction. This is similar to different OH absorption lines observed in direction to W28 (Yusef-Zadeh et al. 2003).

This additional molecular cloud could be of any size. The large-scale ¹²CO(1-0) images in Fig. 4 and Fig. 5 do not show any obvious structure that could be associated with this secondary cloud. To investigate this scenario we compared the hydrogen column density derived from OH and CO in the PSR direction. The 3rd panel in Fig. 2 shows the CO emission spectrum which has several components, the last one being centered at 103.2 km s⁻¹. This component has the integrated CO intensity of 75.9 K km s⁻¹. Using the conversion factor between the integrated CO intensity and H₂ column density by Dame et al. (2001) we derive $N(\text{H}_2) = 1.5 \times 10^{23} \text{ cm}^{-2}$ in this direction, or $N_{\text{H}} = 3 \times 10^{23} \text{ cm}^{-2}$. This agrees well with $N_{\text{H}} = 2\text{--}4 \times 10^{23} \text{ cm}^{-2}$ derived from the total OH column density traced by the PSR absorption spectrum and the “pulsar-off” spectrum. This suggests that, most likely, all OH seen in absorption and CO seen in emission coexist in the same region and that the existence of an additional molecular cloud along the line of sight is not very likely explanation.

7.2. All molecular gas is in front of the SNR and the PSR

Another possibility is that the OH absorption features seen in the PSR absorption and “pulsar-off” spectra originate from *the same* general molecular cloud located in front of both the PSR and the SNR. This could happen in the case where the PSR absorption is produced by a small clump (‘cloudlet’), while the shallower, broader absorption features against the SNR are caused by an ensemble of ‘cloudlets’ of varying properties (Fig. 6 case 2). Furthermore, the small ‘cloudlet’ could represent a typical building block for the molecular cloud.

What is particularly interesting about this scenario is that it would be a clear demonstration that a pencil-sharp absorption sample can differ *dramatically* from a large-angle absorption sample. This OH result would be very different from HI absorption findings. Dickey et al. (1979) and Payne et al. (1982) observed continuum sources over a large range of solid angles and compared results to those

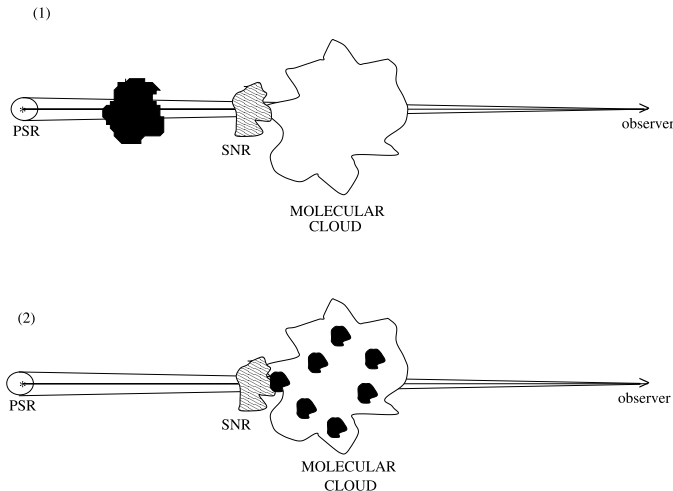


FIG. 6.— Two possible scenarios for the origin of OH absorption lines. (1) An additional molecular cloud (shown in black) is located in front of PSR but behind the SNR producing the PSR absorption spectra (shown in Fig. 1). The PSR absorption spectra measure absorption only in the tiny column in front of the PSR (illustrated as a line), while the “pulsar-off” spectra (shown in Fig. 2) measure absorption (and emission) throughout the illustrated cone that covers a portion of the SNR (FWHM ~ 2 arcmin). (2) All molecular gas is in front of both the SNR and the PSR. The PSR absorption features are produced by one small clump (‘cloudlet’) while the shallower, broader absorption against the SNR is produced by an ensemble of small clumps (shown in black).

against small solid-angle sources. They found no obvious difference. Dickey et al. (1981) observed 21-cm absorption in front of pulsars and extragalactic sources of widely varying angular sizes and concluded that the statistics of absorption are similar in all cases, and that the ‘cloudlet’ model of the interstellar HI is not prominent. However, the difference at HI and OH would not be totally unexpected: the solid-angle effect is expected to be more pronounced for molecular gas where clumpiness is known to be significant.

We explore some of the consequences of this scenario in the following two subsections.

7.2.1. An estimate of the ‘cloudlet’ size

The solid angle subtended by the ‘cloudlet’ intercepts solid angles of both PSR and SNR continuum emission regions (Fig. 5). However, the “pulsar-off” spectrum does not appear to have a significant contribution from the ‘cloudlet’ seen in the PSR absorption spectrum. This suggests that the ‘cloudlet’ covers a very small fraction of the SNR and can be used to place an upper limit on the ‘cloudlet’ size.

In this particular scenario, when all molecular gas is located in front of both the PSR and the SNR, the observed optical depth profile against the SNR (τ_{SNR} , shown in Fig. 2) is a solid angle weighted average of the ‘cloudlet’ optical depth profile, which we will assume to be the same as the PSR optical depth profile (τ_c , shown in Fig. 1), and the pure optical depth profile against the SNR (τ'_{SNR}) that would be uncontaminated by the ‘cloudlet’ absorption:

$$\frac{\Omega'_{\text{SNR}}\tau'_{\text{SNR}} + \Omega_c\tau_c}{\Omega'_{\text{SNR}} + \Omega_c} = \tau_{\text{SNR}}. \quad (3)$$

Here, Ω'_{SNR} and Ω_c are solid angles of the SNR and PSR continuum emission occupied by OH seen in absorption. We assume that $\tau_{\text{SNR}} = k\tau'_{\text{SNR}}$, where k is determined from comparison of our OH observations with previous ones. Previous OH observations of G33.6+0.1 were obtained with much larger telescope beams covering the whole SNR

(Turner 1979; Green 1989) and therefore averaging optical depth profiles over larger solid angles. Hence these spectra can be assumed to be τ'_{SNR} . Our OH spectra agree with previous observations within 60% (see Section 3.1.2), meaning that $k \geq 1.6$. If we assume that Ω'_{SNR} is less or equal a half of the solid angle subtended by the Arecibo beam (as suggested in Fig. 5), then the peak optical depths listed in Table 1 allow us to place an estimate of $\Omega_c \leq 0.25$ arcmin².

At the distance of 7 kpc Ω_c translates to a maximum linear size of 1 pc for the OH absorbing ‘cloudlet’. Using the values for $N_{\text{OH}}/T_{\text{ex}}$ from Table 1, we can now estimate the total column density of hydrogen in the ‘cloudlet’, and from there its volume density (n). Under assumption of a simple spherical geometry, $n = N_{\text{OH}}/(4 \times 10^{10} \times r_{\text{pc}})$, and $T_{\text{ex}} \approx 10$ K, we estimate $n > 10^5$ cm⁻³. The hydrogen volume density and ‘cloudlet’ size suggest that this is a very small and dense cloud of molecular gas, similar to the tiny-scale molecular features on sizes of order of 10 AU discovered by Moore & Marscher (1995).

7.2.2. Modeling optical depth profiles

We now investigate the possibility that the ‘cloudlet’, seen in the PSR absorption spectra, represents a typical building block for the molecular cloud by attempting to model broad absorption lines in the “pulsar-off” spectra with an ensemble of narrow absorption lines from the PSR absorption spectra.

We use a simple model for modeling optical depth profiles, based on the idea from Marscher, Bania & Wang (1991). The model assumes a random distribution of a large number of ‘cloudlet’ absorption features within boundaries of the molecular cloud. While ‘cloudlets’, or basic building blocks, have thermal linewidths, the observed final broad linewidths in the “pulsar-off” spectra are due to the bulk motion of individual ‘cloudlets’. We represent the ‘cloudlet’ optical depth spectrum (τ_c) with a Gaussian function, having the peak optical depth (τ_{max}), and the standard deviation (σ_c in km s⁻¹). ‘Cloudlet’

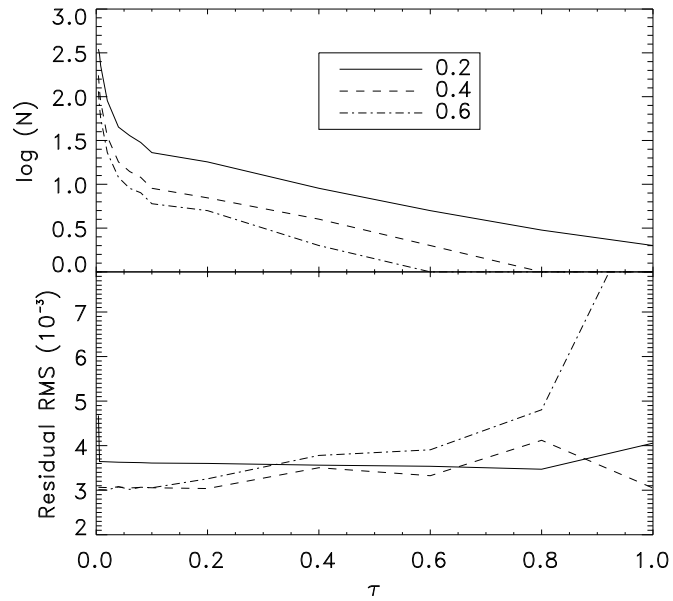


FIG. 7.— Bottom: rms of (modeled optical depth profile – SNR optical depth profile at 1665 MHz) as a function of peak optical depth of the template optical depth profile (τ_{\max}). Top: Natural logarithm of the number of template optical depth profiles necessary to model the SNR optical depth profile at 1665 MHz as a function of peak optical depth of the template optical depth profile.

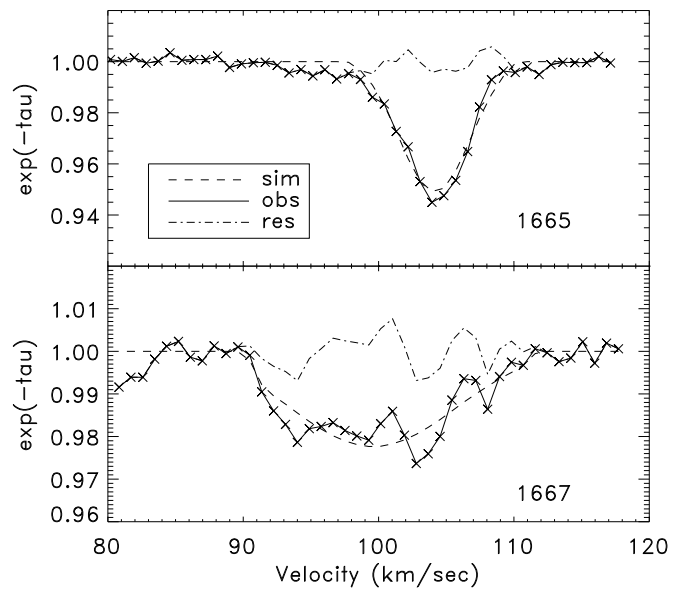


FIG. 8.— The best modeled optical depth profiles obtained for the case of $\sigma_c = 0.4 \text{ km s}^{-1}$ and $\tau_{\max} = 0.05$. Observed data are shown with solid line, modeled with dashed line, and the residuals are shown as dot-dashed line.

optical depth profiles are centered along the line-of-sight according to the probability distribution function. We use a Gaussian form for this function which is determined by fitting a single normalized Gaussian function to the ‘‘pulsar-off’’ optical depth profile.

The velocity interval of interest, ΔV , is then divided into $\Delta V/2\sigma_c$ velocity bins, each of width $2\sigma_c$. The probability that each velocity bin contains 0, 1, 2, ... or N ‘cloudlet’ optical depth profiles is given by the binomial statistics, and the expected value of $e^{-\tau}$, averaged over $\Delta V/2\sigma_c$ velocity bins, can be calculated using:

$$\langle e^{-\tau} \rangle = \frac{2\sigma_c}{\Delta V} \sum_{i=1}^{\Delta V/2\sigma_c} q_i^N \left[\sum_{j=0}^N \binom{N}{j} \left(\frac{p_i}{q_i} \right)^j e^{-j\tau_c} \right] \quad (4)$$

or

$$\langle e^{-\tau} \rangle = \frac{2\sigma_c}{\Delta V} \sum_{i=1}^{\Delta V/2\sigma_c} (p_i e^{-\tau_c} + q_i)^N. \quad (5)$$

Here, p_i is the probability that the central velocity of a ‘cloudlet’ belongs to the i th velocity bin, which is estimated from the probability distribution function, while $q_i = (1 - p_i)$. We have experimented with different velocity intervals ΔV and the best results are achieved for $\Delta V \sim 2.0 \times \text{FWHM}$ of the single Gaussian fit to the ‘‘pulsar-off’’ optical depth profile.

The simulations were performed for $\sigma_c = 0.2 \text{ km s}^{-1}$, the internal thermal velocity dispersion for gas with kinetic temperature of about 100 K. This kinetic temperature was suggested by the HI absorption and emission data toward B1849+00 from Frail & Clifton (1989). In addition, we allowed a slight broadening of the internal ‘cloudlet’ velocity dispersion and performed simulations for $\sigma_c = 0.4$ and 0.6 km s^{-1} . The last value is particularly of interest as it corresponds to the standard deviation of the PSR absorption line from Table 1, while $\sigma_c = 0.4 \text{ km s}^{-1}$ is an intermediate value between the pure thermal and the PSR linewidths. For each value of σ_c and the range of τ_{max} from 0.004 to 2.0, we estimated $\langle e^{-\tau} \rangle$ for various N (ranging from 1 to 250). The simulated (expected) optical depth spectrum was then compared with the original SNR spectrum, residuals were determined and the rms of residuals was calculated. The best model fit was assumed to correspond to the lowest rms residual value and the corresponding number of clumps, N , was taken as the best estimate. For a given range of τ_{max} , Fig. 7 shows the rms of residuals and the best number of clumps determined for the 1665 MHz SNR optical depth profile, when $\sigma_c = 0.2$ (solid line), 0.4 (dashed line) and 0.6 km s^{-1} (dot-dashed line).

The results of simulations show several general trends: the rms of residuals slowly increases with τ_{max} ; number of clumps needed to fit the SNR profile increases when τ_{max} decreases; and number of clumps also increases when σ_c decreases. In the case of $\sigma_c = 0.4$ or 0.6 km s^{-1} , the simulated spectra are unsatisfactory (have high residual rms) for $\tau_{\text{max}} > 0.6$. In the case of $\sigma_c = 0.2 \text{ km s}^{-1}$ the rms stays quite stable all the way to $\tau_{\text{max}} \sim 0.8$. The lowest rms of residuals are achieved for $\tau_{\text{max}} < 0.1$ and $\sigma_c = 0.4$ or 0.6 km s^{-1} . Although good fits (small rms) are achieved for the wide parameter space given by $\tau_{\text{max}} \leq 0.6$ and any σ_c , the number of required ‘cloudlets’ is too small, less than 10, in most cases where $\tau_{\text{max}} > 0.1$.

For the case of $\sigma_c = 0.4$ or 0.6 km s^{-1} , a large number of ‘cloudlets’ could make the molecular cloud only under very low peak optical depth conditions of $\tau_{\text{max}} \sim 0.02 - 0.03$. The most meaningful results are achieved for the thermal velocity dispersion, $\sigma_c = 0.2 \text{ km s}^{-1}$ with $\tau_{\text{max}} < 0.1$, where > 30 ‘cloudlets’ are needed to model well the SNR optical depth profiles. Typical τ_{max} obtained from surveys against extragalactic sources (Dickey et al. 1981; Colgan et al. 1989; Liszt & Lucas 1996) is around 0.05. As an example of how well optical depth profiles can be modeled, we show the case for $\sigma_c = 0.4 \text{ km s}^{-1}$ and $\tau_{\text{max}} = 0.05$ in Figure 8. Although this is a very simple geometrical model it is possible to model SNR spectra surprisingly well. However, the 1665 MHz modeled profile is missing line wings, while the 1667 MHz profile is extremely complex. If the thermal ‘cloudlet’ linewidth is used, $N \sim 50$ is required.

As a conclusion, the required number of ‘cloudlets’, with properties similar to the PSR optical depth profile, necessary for building the SNR profile is too small. The PSR profiles hence can not be building blocks. Models of a large number of ‘cloudlets’ having optical depth profiles with thermal linewidth and $\tau_{\text{max}} < 0.1$ could work well.

8. SUMMARY

We have detected OH absorption against PSR B1849+00 at both 1665 and 1667 MHz OH mainlines using the Arecibo telescope. This is the first successful detection of OH in both mainlines toward any pulsar. The most important aspect of this detection is that it opens up a new avenue for studying properties of molecular gas using extremely small solid angle background sources. The OH absorption features detected against B1849+00 are unusually deep ($\tau = 0.9$ at 1667 MHz) and narrow (FWHM=1.1 km s^{-1}). High OH optical depths are often found close to SNRs but with wide linewidths that indicate an interaction between a SNR and a molecular cloud.

In addition, we have detected several absorption and emission features against G33.6+0.1, a nearby SNR that is partially covered by the Arecibo beam. The most interesting result of this study is that a pencil-sharp absorption sample probed by the PSR differs greatly from the large-angle absorption sample probed by the SNR along the same line-of-sight. In trying to understand this difference we have obtained $^{12}\text{CO}(1-0)$ observations of G33.6+0.1 with the 12-m telescope.

We have investigated two geometrical scenarios in order to explain the observed OH absorption spectra. In the first scenario, an additional molecular cloud, located in front of the PSR but behind the SNR, could be responsible for the pencil-sharp absorption sample probed by the PSR. The main implication of the second scenario, whereby the OH absorption against the PSR and the SNR originate from the same molecular cloud, is that the statistics of OH absorption depend greatly on the size of the background sources. This result is different from what was found for the case of HI absorption studies, but not totally unexpected as clumpiness of molecular gas is known to be significant. We have further shown that in this scenario, the PSR is most likely probing a very small molecular clump, ‘cloudlet’, having angular size of < 30 arcsec and hydrogen volume density $> 10^5 \text{ cm}^{-3}$.

We have also investigated the possibility that the ‘cloudlet’ represents a typical building block for the molecular cloud by modeling the SNR OH absorption profiles with template ‘cloudlet’ opacity profiles. It was shown that this is not the case, however the SNR OH absorption profiles can be modeled well with template profiles having peak opacity of <0.1 and velocity dispersion of $\sim 0.2\text{--}0.4$ km s $^{-1}$. High velocity and spatial resolution OH mapping of the whole SNR is desirable to distinguish further between the two possible scenarios. In addition, further OH absorption measurements toward other pulsars are important to constrain how common such phenomenon may be.

We would like to express our thanks to Caltech’s Center for Advance Computation and Research for the use of their facilities for data storage and processing. We appreciate greatly Rick Jenet’s help with processing of raw pulsar data. S. S. is grateful to Alberto Bolatto and Jonathan Swift for valuable input on the 12-m observing and data reduction strategy. S. S. would also like to thank all staff members of the 12-m telescope for their great support and help. We are grateful to an anonymous referee for helpful suggestions. The National Radio Astronomy Observatory is a facility of the National Science Foundation operated under cooperative agreement by Associated Universities, Inc.

REFERENCES

- Bourke, T. L., Myers, P. C., Robinson, G., & Hyland, A. R. 2001, *ApJ*, 554, 916
 Brooks, K. J. & Whiteoak, J. B. 2001, *MNRAS*, 320, 465
 Caswell, J. L., Milne, D. K., & Wellington, K. J. 1981, *MNRAS*, 195, 89
 Clifton, T. R., Frail, D. A., Kulkarni, S. R., & Weisberg, J. M. 1988, *ApJ*, 333, 332
 Clifton, T. R. & Lyne, A. G. 1986, *Nature*, 320, 43
 Colgan, S. W. J., Salpeter, E. E., & Terzian, Y. 1989, *ApJ*, 336, 231
 Cordes, J. M. & Lazio, T. J. W. 2002, *ApJ*, in press
 Dame, T. M., Hartmann, D., & Thaddeus, P. 2001, *ApJ*, 547, 792
 Deshpande, A. A. & Ramachandran, R. 1998, *MNRAS*, 300, 577
 Dickey, J. M., Crovisier, J., & Kazes, I. 1981, *A&A*, 98, 271
 Dickey, J. M., Terzian, Y., & Salpeter, E. E. 1979, *ApJ*, 228, 465
 Fich, M., Blitz, L., & Stark, A. A. 1989, *ApJ*, 342, 272
 Flower, D. R. & Pineau des Forets, G. 1998, *MNRAS*, 297, 1182
 Frail, D. A. & Clifton, T. R. 1989, *ApJ*, 336, 854
 Frail, D. A., Weisberg, J. M., Cordes, J. M., & Mathers, C. 1994, *ApJ*, 436, 144
 Galt, J. A. 1974, *A&A*, 31, 235
 Goss, W. M. 1968, *ApJS*, 15, 131
 Green, A. J., Frail, D. A., Goss, W. M., & Otrupcek, R. 1997, *AJ*, 114, 2058
 Green, D. A. 1989, *MNRAS*, 238, 737
 Green, D. A. & Dewdney, P. E. 1992, *MNRAS*, 254, 686
 Han, J. L. 1997, *A&A*, 318, 485
 Heiles, C. 1997, *ApJ*, 481, 193
 Helfer, T. T. & et al. 2003, *ApJS*, in press
 Jenet, F. A., Cook, W. R., Prince, T. A., & Unwin, S. C. 1997, *PASP*, 109, 707
 Koralesky, B., Frail, D. A., Goss, W. M., Claussen, M. J., & Green, A. J. 1998, *AJ*, 116, 1323
 Koribalski, B., Johnston, S., Weisberg, J. M., & Wilson, W. 1995, *ApJ*, 441, 756
 Löhmer, O., Kramer, M., Mitra, D., Lorimer, D. R., & Lyne, A. G. 2001, *ApJ*, 562, L157
 Liszt, H. & Lucas, R. 1996, *A&A*, 314, 917
 Lyne, A. G., Manchester, R. N., & Taylor, J. H. 1985, *MNRAS*, 213, 613
 Manchester, R. N. & Gordon, M. A. 1971, *ApJ*, 169, 507
 Marscher, A. P., Bania, T. M., & Wang, Z. 1991, *ApJ*, 371, L77
 Marscher, A. P. & Stone, A. L. 1994, *ApJ*, 433, 705
 Moore, E. M. & Marscher, A. P. 1995, *ApJ*, 452, 671
 Payne, H. E., Terzian, Y., & Salpeter, E. E. 1982, *ApJS*, 48, 199
 Scoville, N. Z., Yun, M. S., Sanders, D. B., Clemens, D. P., & Waller, W. H. 1987, *ApJS*, 63, 821
 Seward, F., Slane, P., Smith, R., & Sun, M. 2002, *ApJ*, in press
 Slysh, V. I. 1972, *Astronomicheskii Cirkular*, 731, 28
 Spangler, S. R., Mutel, R. L., Benson, J. M., & Cordes, J. M. 1986, *ApJ*, 301, 312
 Taylor, J. H., Manchester, R. N., & Lyne, A. G. 1993, *ApJS*, 88, 529
 Ter Meulen, J. J. & Dymanus, A. 1972, *ApJ*, 172, L21+
 Turner, B. E. 1979, *A&AS*, 37, 1
 Weisberg, J. M., Boriakoff, V., & Rankin, J. 1979, *A&A*, 77, 204
 Weisberg, J. M., Siegel, M. H., Frail, D. A., & Johnston, S. 1995, *ApJ*, 447, 204
 Yusef-Zadeh, F., Wardle, M., & Roberts, D. A. 2003, *ApJ*, 583, 267